Journal of Materials Chemistry B

ROYAL SOCIETY OF CHEMISTRY

PAPER

View Article Online
View Journal | View Issue

Cite this: J. Mater. Chem. B, 2025, 13, 8897

Improving extracellular matrix penetration with biocatalytic metal–organic framework nanoswimmers†

Qianfan Chen,[ac] Si Liu,[bc] Peijun Qin,[a] Jueyi Xue,[bc] Peiji Deng,[bc] Ziping Li,[bc] John Whitelock,[a] Tianruo Guo[a] and Kang Liang *[abc]

Received 7th March 2025,
Accepted 27th May 2025

DOI: 10.1039/d5tb00509d

rsc.li/materials-b

The development of self-propelled nanomotors offers a promising strategy to enhance targeted drug delivery efficiency in cancer therapy. Active motion is believed to aid nanomotors in overcoming the physical barriers of the tumor microenvironment, allowing for deep tissue penetration; however, this crucial concept lacks detailed mechanistic understanding. In this study, we report catalase and collagenase dual-enzyme functionalized zeolitic imidazolate framework-90 (ZIF-90) nanomotors. Catalase enables the nanomotors with self-propulsion in the presence of low amount of hydrogen peroxide, while collagenase enables catalytic decomposition of collagen, a major component of the extracellular matrix (ECM), thereby enhancing motility and facilitating deeper penetration into the ECM. Experimental and computational studies elucidated the detailed mechanisms governing ECM penetration kinetics. Using a three-dimensional tumor spheroid model, the nanomotors demonstrated enhanced tissue penetration, leading to improved drug delivery and a significant reduction in cell viability. These findings underscore the potential of self-propelled nanomotors to improve drug delivery efficiency in solid tumors by leveraging both biocatalytic activity and active motion to navigate biological barriers.

Introduction

Over the past several decades, significant advancements have been made in the treatment of numerous complex and long-standing diseases, leading to the development of novel therapeutics for previously untreatable conditions. However, many of these pharmaceutical interventions continue to present substantial challenges, including adverse side effects such as toxicity to healthy tissues,[1–3] inefficacy in targeting specific pathological sites,[4] and poor bioavailability.[5] For example, many drugs are degraded by endogenous enzymes in the gastrointestinal tract, limiting their effectiveness when administered orally, despite promising *in vitro* results.[6] To overcome these limitations, nanoparticle-based drug delivery systems have emerged as a promising strategy to enhance therapeutic precision and efficacy.

The utilization of nanoscale particles as carriers has the potential to transport therapeutic agents to specific sites within the body,[7] thereby establishing a controlled and precise drug delivery system. These nanoparticles can be engineered with tailored physicochemical and biological properties to enhance drug bioavailability,[8] stability,[9] and facilitate targeted delivery,[10] which improves therapeutic efficacy while minimizing adverse effects. By encapsulating drugs within nanoparticles or conjugating them to the nanoparticle surface, the delivery system protects the active pharmaceutical ingredients from degradation,[11] enhances solubility,[12] and enables controlled release.[13–16] Moreover, nanoparticle-based drug delivery systems can be designed to selectively target diseased tissues or cells, such as tumors, thereby reducing off-target toxicity and improving the overall therapeutic index.[17]

However, once nanoparticles are introduced into the human body, their movement is predominantly passive, as they lack autonomous motility. Furthermore, they encounter various biological barriers prior to reaching the target site.[18] For instance, during cancer progression, malignant cells promote stiffening of the extracellular matrix (ECM), resulting in a more abundant, denser, and rigid matrix.[19] Dysregulation of the ECM is a key distinction between tumor and normal tissues.[20] This altered ECM poses a significant barrier, significantly limiting the penetration of nanoparticles into the interior of tumor tissues,[21,22] thereby limiting their therapeutic efficacy.[23] In fact,

[a] Graduate School of Biomedical Engineering, The University of New South Wales, Sydney 2052, NSW, Australia. E-mail: kang.liang@unsw.edu.au
[b] School of Chemical Engineering, The University of New South Wales, Sydney 2052, NSW, Australia
[c] Australian Centre for NanoMedicine, The University of New South Wales, Sydney 2052, NSW, Australia

† Electronic supplementary information (ESI) available. See DOI: https://doi.org/10.1039/d5tb00509d

statistics show that on average, only about 0.7% of administered nanoparticles successfully reach solid tumors.[24,25]

Recently, artificial micro-/nanoscale motors, commonly referred to as nanoswimmers, have emerged as promising candidates in nanomedicine.[26–32] Nanoswimmers are devices that convert various energy sources into mechanical motion or actuation in liquid environments.[33] Unlike conventional nanoparticles, they exhibit self-propelled motion with defined directionality and velocity, allowing them to execute more complex tasks.[34] Beyond the typical characteristics of conventional passive micro- and nanoparticles, the active motion of nanoswimmers offers tremendous potential for drug delivery, including overcoming biological barriers, enhancing cellular uptake,[35–37] enabling site-directed cell destruction,[38–40] and improving *in vivo* therapeutic efficacy.[41–44] Despite some progress in the development of therapeutic drugs and drug delivery systems in recent years, the penetration of drugs into tumor tissues remains a significant challenge due to the inherent biological barriers of tumors. Although many nanoparticle-based delivery systems rely on enhanced permeability and retention (EPR) effects and targeted delivery to reach tumor regions,[45–48] these approaches are often inadequate in achieving effective tumor coverage.

In this context, while recent research efforts focus on the design of intricate nanoswimmer morphologies and diverse propulsion mechanisms,[49–52] how to enable these nanoswimmers to successfully navigate through the dense ECM remains an unresolved challenge.[53,54] The extracellular matrix not only serves as a physical barrier but also has a complex biochemical structure that limits the effective penetration of nanoparticles. Existing studies mainly focus on optimizing propulsion mechanisms, yet there is a lack of direct visualization and detailed mechanistic understanding of how to effectively overcome this biological barrier and penetrate deeply into the tumor microenvironment. To address this challenge, we have developed a nanoswimmer (i.e. nanomotor) capable of simultaneously degrading the ECM within the tumor microenvironment and propelling itself, thereby significantly enhancing intratumoral drug penetration. This strategy overcomes the limitations of conventional drug delivery systems and advances the application of nanoswimmers for improved tumor therapy.

In this study, we report a catalase and collagenase dual-enzyme-functionalized biocatalytic nanomotor as a model to study ECM penetration. Using ZIF-90 nanoparticles as the structural basis, the nanomotor incorporates catalase, which catalyzes the decomposition of hydrogen peroxide in the surrounding environment, providing propulsion force. Given that collagen constitutes a major component of the ECM,[55] the nanomotor's surface is functionalized with collagenase to biocatalytically degrade collagen, thereby further enhancing its movement through the dense and rigid ECM. Upon reaching tumor cells, the nanomotor achieves targeted drug release through a dual-responsive mechanism sensitive to both pH and ATP levels, thereby enabling effective drug delivery within solid tumor tissues (Fig. 1). This study aims to improve our understanding of the nanomotor's navigational capabilities within the tumor microenvironment, overcoming biological barriers that typically impede the conventional nanoparticle-based drug delivery system.

Materials and methods

Reagents and materials

Polyvinylpyrrolidone (Mw 10 000), imidazole-2-carboxaldehyde (ICA), zinc nitrate hexahydrate, and 3-(4,5-dimethylthiazol-2-yl)-2,5-diphenyltetrazolium bromide (MTT) were purchased from

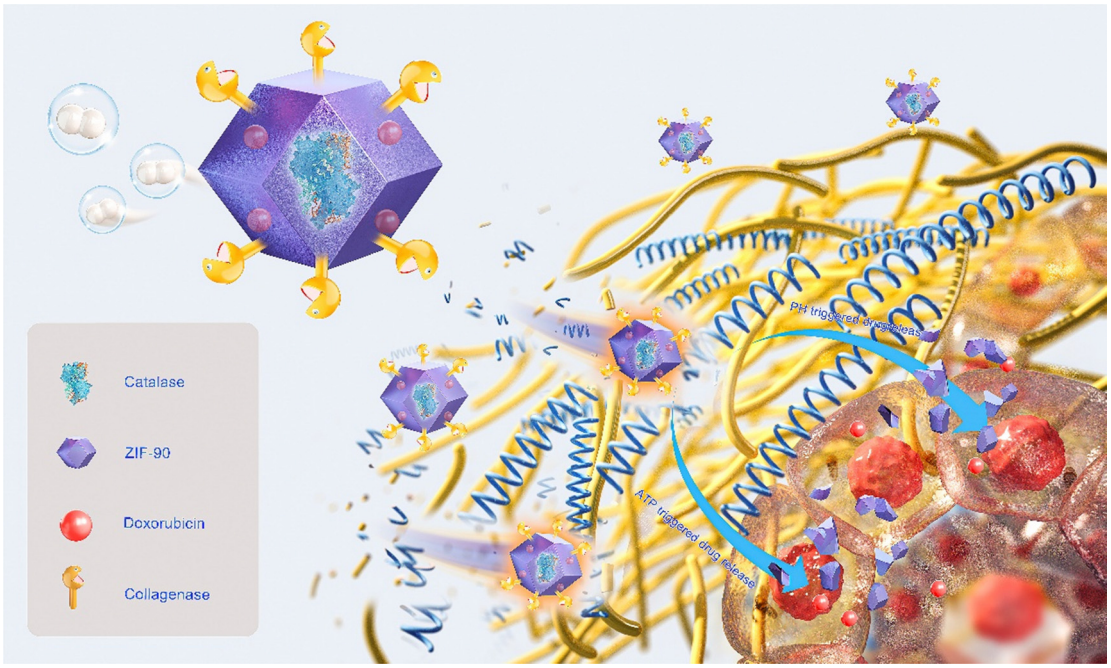

Fig. 1 Schematic diagram of ZIF-90 nanomotors with enhanced ECM penetration.

Merck. Calcein-green and the LIVE/DEAD™ Fixable Violet Dead Cell Stain Kit were obtained from Thermo Fisher Scientific. Matrigel and Transwell inserts were supplied by Corning. All other chemicals were procured from Merck and used without further purification.

Nanomotor fabrication

Synthesis of CAT-COL@ZIF-90-DOX. To synthesize CAT-COL@ZIF-90-DOX, 38.4 mg of ICA and 40 mg of PVP were dissolved in 1 mL of DI water, while a 0.1 M ethanol solution of zinc nitrate was prepared separately. To initiate the reaction, 1 mL of the ICA solution was added to a stirring apparatus, followed by the addition of 200 μL of catalase solution (5 mg mL^{-1}) and 200 μL of DOX solution (5 mg mL^{-1}). After thorough mixing, 1 mL of the zinc nitrate ethanol solution was added, and the reaction mixture was stirred for 15 minutes. The resulting product was centrifuged and washed three times with Milli-Q water, yielding CAT@ZIF-90-DOX. Next, 2 mL of the CAT@ZIF-90-DOX solution was combined with 200 μL of collagenase solution (5 mg mL^{-1}) and 20 μL of $NaCNBH_3$ solution (320 mg mL^{-1} in 1 M NaOH). The mixture was stirred for six hours, then centrifuged and washed three times with Milli-Q water, resulting in the final product, CAT-COL@ZIF-90-DOX.

Motion analysis. Hydrogen peroxide solutions of varying concentrations were added to grooved glass slides, followed by the introduction of fluorescently labeled nanomotors. The nanomotors were observed under a microscope, and images were captured every 100 milliseconds, resulting in a total of 30 images. The nanomotor coordinates were then analyzed using ImageJ to map their trajectories.

Preparation of the collagen film. Before use, the membrane of the standard Transwell device was removed. A layer of Parafilm was then placed at the base of the empty Transwell, and a type I collagen solution (60 μL, 10 mg mL^{-1}) was dispensed onto it. Glutaraldehyde solution (4 μL, 10%) was added as a crosslinking agent. The setup was left to dry at room temperature for 48 hours, after which the Parafilm was carefully removed, leaving a collagen membrane formed on the Transwell framework.

Nanomotor penetration study using Transwell. 4T1 cells were seeded at the bottom of a 24-well plate with prepared 1640 medium (1640: FBS/penicillin/streptomycin = 100 : 10 : 1) and incubated at 37 °C to allow for cell attachment and growth. After 48 hours, the medium was replaced with fresh 1640 medium, and Transwell inserts containing the test material (nanomotors and collagen membrane in 1640 media) were introduced. The cells were co-cultured with the test material for 24 hours. Following the 24-hour exposure, cell viability was assessed using the MTT assay to evaluate the cytotoxic effects of the test material.

A computational model of particle motion. This model focuses on evaluating the penetration efficiency of nanomotors through collagen films of varying thicknesses. All simulations were performed using COMSOL Multiphysics v.6.2 (COMSOL Inc., Burlington, MA), integrating the transport of diluted species and particle tracing for fluid flow physics.

Model geometry. The geometrical parameters of the model were based on the experimental setup. A container filled with an H_2O_2 solution was represented by a rectangular domain, while the collagen film was modelled as a thin rectangular region positioned at the bottom of an internal support structure within the container (Fig. S1, ESI†).

Transport of diluted species physics. The diffusion coefficient and initial concentration of nanomotors were defined using the transport of diluted species physics.

The diffusion coefficient, D, was calculated using the Stokes–Einstein relation:

$$D = \frac{k_B \cdot T}{6\pi\eta r_p} = \frac{1.38 \times 10^{-23}\ \mathrm{J\,K^{-1}} \cdot 300\ \mathrm{K}}{6 \times \pi \times 2 \times 10^{-5}\ \mathrm{Pa\,s} \times 250\ \mathrm{nm}} = 4.39 \times 10^{-11}\ \mathrm{m^2\,s^{-1}}$$

where k_B represents the Boltzmann constant. T denotes the temperature. η represents the dynamic viscosity, and r_p is the nanomotor radius.

The initial nanomotor concentration in all domains was defined as c_{init}, expressed by:

$$c_{init} = c_0 \cdot (1 - \mathrm{flc2hs}(x^2 + y^2 - \mathrm{smooth}^2,\ 5 \times 10^{-11}))$$

where c_0 is the peak initial concentration, and flc2hs( ) is a built-in COMSOL smoothing function for transitioning concentrations. The term $x^2 + y^2 - \mathrm{smooth}^2$ defines a circular region cantered at the origin (top-center of the container), with a radius of smooth. For $x^2 + y^2 < \mathrm{smooth}^2$, the concentration approaches c_0, and for $x^2 + y^2 \geq \mathrm{smooth}^2$, the concentration decreases smoothly to near zero. The concentration variation in the boundary region was controlled by the smoothing parameter 5×10^{-11}, ensuring that the concentration distribution remained continuous and stable during numerical computations. All external container boundaries were set to a concentration of zero.

Particle tracing for fluid flow physics. The container's bottom boundary was defined as a freeze wall to simulate nanomotor interactions with 4T1 cells. An inlet was placed at the upper boundary of the support structure, representing the initial deployment of nanomotors. The release time was set as range (0, 0.1, 1000), indicating uniform intervals between 0 and 0.1 seconds. The nanomotor velocity was defined as:

$$[x, y] = [\mathrm{speed} \cdot \mathrm{sign}_x \cdot \cos(\theta),\ \mathrm{speed} \cdot \mathrm{sign}_y \cdot \sin(\theta)]$$

This equation represents the nanomotors' two-dimensional motion. The upper boundary of the rectangular region representing the collagen film was assigned a pass-through condition of 0.01%, allowing a small probability of penetration upon contact, with all other interactions modelled as elastic rebounds. All remaining boundaries were set as bounce wall conditions.

The total force on each particle, F_{total}, was represented as:

$$F_{total} = F_{drag} + F_{brownian} + F_{gravity}$$

F_{drag} simulated viscous and inertial resistance from the H_2O_2 solution and the collagen film, implemented using the drag force feature. Random ionic Brownian motion ($F_{brownian}$) and gravitational effects ($F_{gravity}$) were defined using the Brownian

Table 1 Model parameters

Symbol	Value	Unit	Description
Heta	2×10^{-5}	Pa s	Dynamic viscosity of H_2O_2
Feta	6×10^{-2}	Pa s	Dynamic viscosity of collagen film
D_p	1050	kg m^{-3}	Density of particle
D_m	10	mg cm^{-3}	Density of collagen film
M	6.87×10^{-17}	Kg	Particle weight
V	5×10^{-6}	m s^{-1}	Particle speed

force and gravity force features, respectively. Relevant parameters are summarized in Table 1.

Mesh setting. A customized mapped mesh was used to create structured rectangular elements, with maximum and minimum element sizes set to 0.05 mm and 7.5×10^{-4} mm, a maximum element growth rate of 1.2, a curvature factor of 0.3, and a narrow region resolution of 1. Additional free triangular mesh was applied as an auxiliary support for regions that could not be covered by the mapped mesh. The complete mesh consisted of 40 150 domain elements and 1254 boundary elements.

The simulation outcomes were visualized through trajectory distribution graphs and penetration–time curves, offering insights into the dynamic interaction between ZIF-90 and the collagen membrane under varying experimental conditions.

Nanomotor penetration study using the spheroid model. Matrigel stored at −20 °C was thawed by placing it on ice and transferring it to a 4 °C refrigerator for 24 hours. Once thawed, the Matrigel was mixed with 4T1 cell culture medium at a 10 : 1 ratio. A volume of 50 μL of the resulting mixture was dispensed into the bottom of each well of a 24-well plate. The plate was inverted and incubated at 37 °C for 1 hour to allow the Matrigel to solidify. After solidification, 1 mL of 1640 medium was carefully added to each well, and the plate was incubated at 37 °C for 48 hours to promote spheroid formation. Following the incubation, the medium was replaced with fresh culture medium with 10 mM H_2O_2, and nanomotors were introduced. The cells were co-cultured with the nanomotors for 24 hours. After the 24-hour co-culture period, cell viability was assessed using the MTT assay to evaluate the penetration efficiency and therapeutic impact of the nanomotors within the spheroid model.

Cell viability assessment using the MTT assay. Before the viability assay, the culture medium was aspirated. The cells were gently washed with PBS to remove any residual compounds that could interfere with the assay. A freshly prepared MTT solution (0.5 mg mL^{-1} in 1640 medium) was then added to each well (100 μL per well). The plate was incubated at 37 °C in the dark for 2 to 4 hours to allow for the formation of formazan crystals. Following incubation, the MTT-containing medium was carefully aspirated, and 1 mL of DMSO was added to each well to dissolve the formazan crystals. The absorbance of the resulting solution was measured at 570 nm using a plate reader, providing a quantitative assessment of cell viability.

Cell staining. Calcein and violet dead cell stain were used to stain 4T1 cells embedded in Matrigel. Both dyes were diluted 1 : 1000 in 1640 culture medium without FBS or P/S. The medium in the 24-well plates was replaced with the dye-containing medium, and the samples were incubated at 37 °C for 12 hours. After incubation, the medium was carefully removed, and the Matrigel surface was gently washed with PBS to remove excess dye. The stained 4T1 cells were then imaged using a confocal microscope for analysis.

Characterization. Powder X-ray diffraction (XRD) patterns were measured on an Empyrean (PANalytial) Bragg–Brentano geometry-ray diffractometer equipped with Cu Kα radiation (λ = 1.54178 Å). Fourier transform infrared (FT-IR) spectroscopy was performed on a Bruker ALPHA-P FTIR spectrometer (diamond ATR). Field-emission scanning electron microscopy (FE-SEM) was carried out with a FEI Nova NanoSEM 450 scanning electron microscope at an acceleration voltage of 5 kV and a spot size of 3.0. Transmission electron microscopy (TEM) images were acquired on a FEI Tecnai G2 T20 transmission electron microscope. Fluorescence intensity and UV-Vis absorbance measurements were carried out on a BMG Labtech Clariostar plate reader in a 96-well setting. Fluorescence microscopy was performed on an inverted optical microscope (Olympus IX53) equipped with an oil immersion 60× objective, a CMOS camera (optiMOS) and a mercury burner (Olympus U-RFL-T). The captured images were processed by FIJI (ImageJ) software. pH was measured on a SevenCompact™ pH/Ion meter with an InLab Micro pH electrode. Dynamic light scattering (DLS) was performed on a Zetasizer Nano ZS (PANalytical), with a refractive index of 1.336 set for the liposome samples.

Results and discussion

Synthesis and characterization of the catalase-collagenase@ZIF-90 (CAT-COL@ZIF-90) nanomotor

A one-pot method is employed to encapsulate catalase (CAT) and anti-cancer drug doxorubicin (DOX) within ZIF-90 nanoparticles (see Methods section)[56] followed by surface functionalization of the collagenase (COL) enzyme through reductive amination. The amino groups of collagenase were first reacted with aldehyde groups on the ZIF-90 surface to form reversible Schiff base linkages. The reaction mixture was then treated with sodium cyanoborohydride to reduce the Schiff bases, thereby stabilizing the linkages as secondary amine bonds. Scanning electron microscopy (SEM) and transmission electron microscopy (TEM) analysis of the synthesized nanoparticles revealed that the synthesized ZIF-90 nanoparticles exhibit a well-defined crystal morphology, with particle sizes ranging from approximately 300 to 800 nm, consistent with previous reports[57] (Fig. 2). Upon enzyme loading, the surface of the ZIF-90 nanoparticles became rough, nevertheless, they still retained the original rhombic dodecahedral morphology (Fig. S2, ESI†). Powder X-ray diffraction (PXRD) analysis was conducted on various ZIF-90 nanoparticles (Fig. 2c), with each sample exhibiting diffraction patterns consistent with standard ZIF-90 XRD data. This further verified that the structural integrity of ZIF-90 remained intact after the incorporation of catalase and collagenase. To confirm the successful encapsulation of catalase and

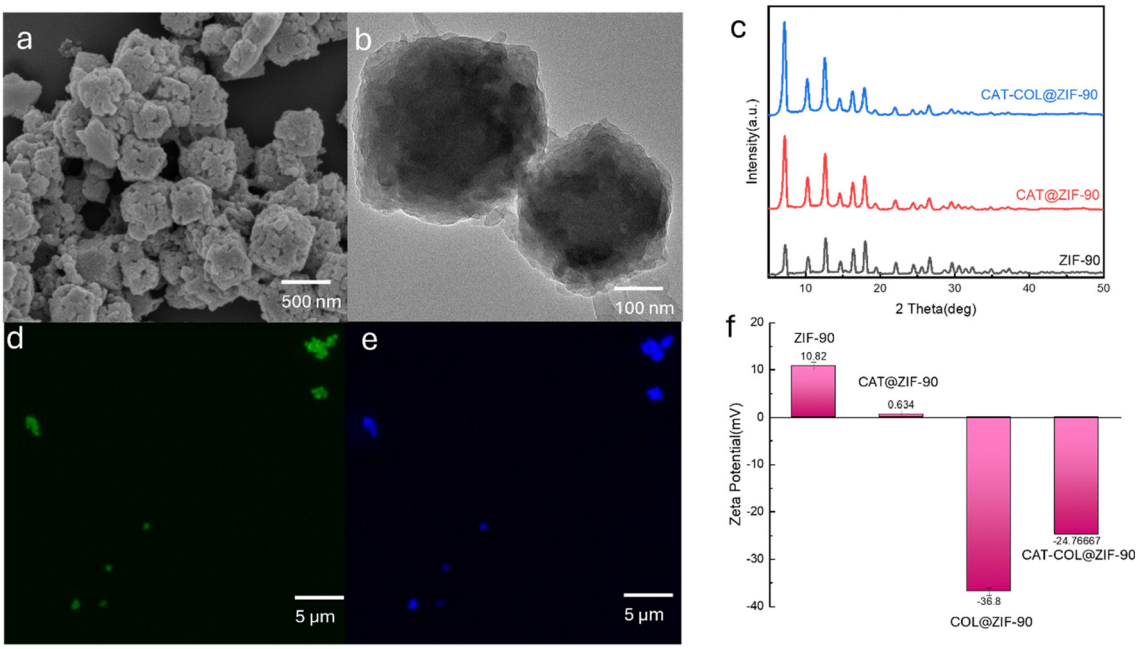

Fig. 2 Characterization of nanomotors. (a) SEM and (b) TEM images of CAT-COL@ZIF-90. (c) PXRD spectra of ZIF-90, CAT-COL@ZIF-90 and CAT-COL@ZIF-90-DOX. (d) and (e) CLSM images of CAT-COL@ZIF-90 (green = FITC-catalase and blue = atto633-collagenase). (f) Zeta potential of ZIF-90, CAT@ZIF-90, COL@ZIF-90 and CAT-COL@ZIF-90.

surface functionalization of collagenase on ZIF-90, catalase and collagenase were fluorescently labelled with FITC and atto-633, respectively, prior to integration with ZIF-90. Confocal laser scanning microscopy (CLSM) images revealed green fluorescence from catalase (Fig. 2d) and blue fluorescence from collagenase (Fig. 2e). Overlaying the two images revealed co-localized fluorescence signals, which matched the positions observed in the bright-field CLSM images of the nanomotors, confirming the successful loading of both enzymes onto the ZIF-90 nanoparticles (Fig. S3, ESI†). Furthermore, FTIR analysis was conducted to confirm the encapsulation of catalase within ZIF-90. The FTIR spectra (Fig. S4, ESI†) revealed the appearance of a new characteristic peak at 1580 nm in catalase-loaded ZIF-90, which corresponds to the N–H bending and C–N stretching (amide II) in catalase. This result provides strong evidence for the successful incorporation of catalase into the ZIF-90 framework. In addition, the surface zeta potential of the ZIF-90 nanomotors was measured at different synthesizing stages (Fig. 2f). Pure ZIF-90 nanoparticles exhibited a positive surface charge, which decreased to close to neutral after encapsulating the negatively charged CAT. The surface potential was further reduced after the attachment of negatively charged COL. The loading efficiency of CAT and COL was calculated to be 74% and 53.8% (Fig. S5, ESI†), respectively, using calibration curves obtained from a fluorescence spectrophotometer.[58]

The subsequent step involves assessing the motility of the nanomotors. The nanomotor utilizes hydrogen peroxide from the surrounding environment as a chemical fuel, with the encapsulated catalase within ZIF-90 catalyzing the decomposition of hydrogen peroxide, thereby generating oxygen nanobubbles.[59] These bubbles, as they escape from the interior of the ZIF-90 nanoparticles, produce a propulsive force that enhances the Brownian motion of the nanomotor, enabling it to achieve greater displacement.[60] Catalase-loaded ZIF-90 was introduced into hydrogen peroxide solutions with varying concentrations. The optical dissolved oxygen meter was used to monitor the oxygen concentration in the solution in real time, and the data were recorded and organized using a computer. The results demonstrated that as the concentration of hydrogen peroxide increased, the rate of oxygen generation also escalated (Fig. 3a). We mixed ZIF-90 particles and catalase-loaded ZIF-90 particles with both water and hydrogen peroxide solutions, respectively. The experimental results showed that only the catalase-loaded ZIF-90 particles caused an increase in oxygen concentration when mixed with hydrogen peroxide (Fig. S6, ESI†), indicating that the catalase encapsulated within the nanomotors retained its catalytic activity. Hydrogen peroxide solutions of varying concentrations (0 mM, 50 mM, 100 mM, and 200 mM) were introduced into grooved glass slides (Fig. S7, ESI†), followed by the addition of a small quantity of fluorescently labeled nanomotors. The movement trajectories of the nanomotors were observed and recorded using fluorescence microscopy. Images were captured at 100-millisecond intervals, with a total of 30 images taken. Subsequently, the coordinates of the nanomotor were recorded using ImageJ software to map the trajectory. It was observed that as the concentration of hydrogen peroxide increased, the activity of the nanomotor was significantly enhanced. (Fig. 3b; for motion tracking of benchmarking samples, see Fig. S8–S11, ESI†). By dividing the displacement by the time, the speed of the nanomotor was determined, and the average speed was calculated from ten individual nanomotors at

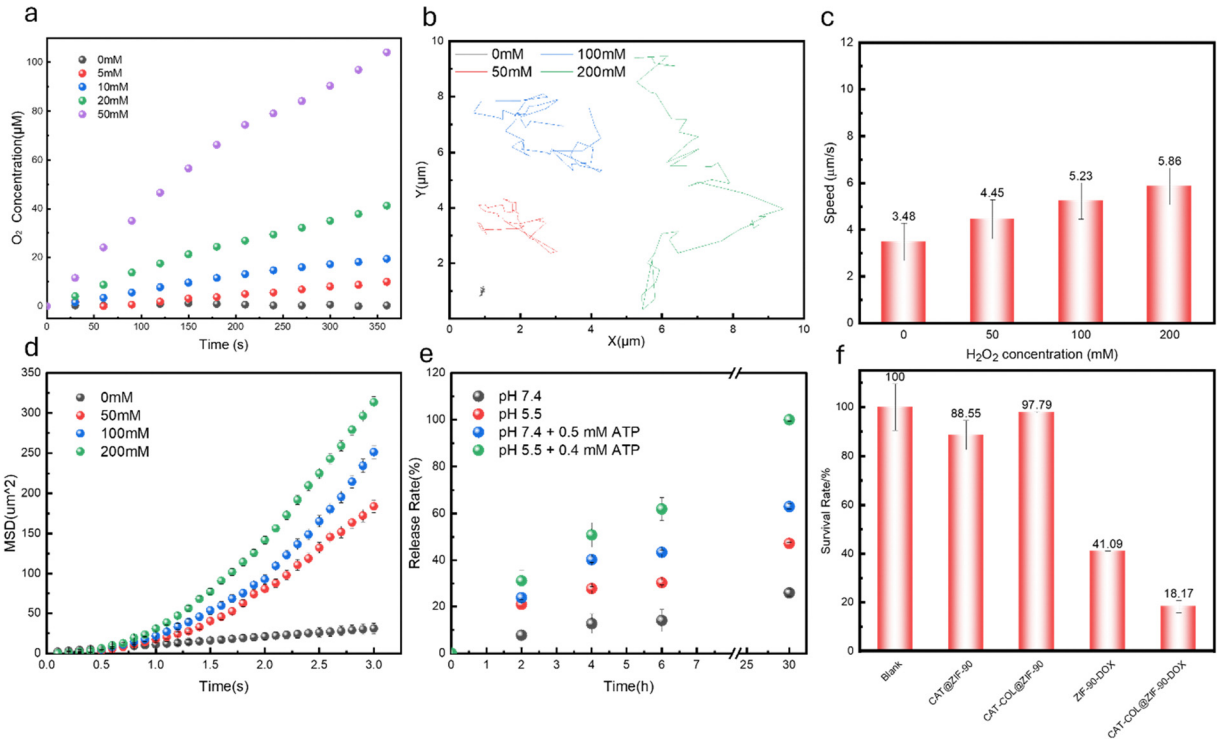

Fig. 3 Motion analysis. (a) Dissolved oxygen *vs.* time as a result of the catalase decomposition of H_2O_2. (b) Movement trajectories of nanomotors at different H_2O_2 concentrations. (c) Average speed and (d) mean squared displacement of nanomotors at different H_2O_2 concentrations. (e) DOX release rate under different conditions. (f) Cell survival rates after treatment with different ZIF-90 compositions after 24 hours.

each concentration, resulting in a plot of nanomotor speed as a function of hydrogen peroxide concentration (Fig. 3c). These results demonstrate a positive linear relationship between the nanomotor's speed and increasing hydrogen peroxide concentration. Additionally, a mean squared displacement (MSD) analysis was performed, which demonstrated that the diffusion capability of the nanomotor increases as the hydrogen peroxide concentration increases (Fig. 3d). To further investigate the effect of hydrogen peroxide solution on the motion of different nanomotors, we mixed ZIF-90, CAT@ZIF-90, COL@ZIF-90, and CAT-COL@ZIF-90 with a 200 mM hydrogen peroxide solution and performed motion tracking. The experimental results showed that nanomotors containing catalase exhibited significantly higher motion speeds compared to those without catalase in the hydrogen peroxide solution (Fig. S12, ESI†). These findings illustrate that the nanomotor is capable of transducing chemical energy from its ambient environment into kinetic energy. This process not only augments its motility but also improves its diffusion efficacy within the surrounding medium.

Given the role of the nanomotor in drug delivery, evaluating its drug release capability is crucial. ZIF-90 exhibits dual responsiveness to pH and adenosine triphosphate (ATP),[25] undergoing structural disintegration in acidic environments or in the presence of ATP, thereby facilitating the release of encapsulated drugs. The release kinetics of DOX from the nanomotor were examined under four distinct conditions (Fig. 3e). In a mild acidic environment with ATP, drug release was maximized, achieving complete release within 30 hours. Conversely, in a neutral solution, the release rate was minimal, with only approximately 20% of the drug released over 30 hours. To further validate this result at the cellular level, the nanomotors were co-cultured with tumor cells and subsequently observed under a microscope. Catalase (green) and collagenase (blue) were pre-labeled with fluorescent dyes to enable visualization of their spatial distribution around the cells. As shown in Fig. S13 (ESI†), the clear separation of green and blue fluorescence signals confirms the disassembly of the nanomotors, thereby facilitating the release of the encapsulated therapeutic agents.

To evaluate the cytotoxic potential of DOX-loaded ZIF-90 on tumor cells and to assess the inherent toxicity of ZIF-90 itself, we co-cultured varying formulations of ZIF-90 particles with 4T1 cells, subsequently measuring cell viability after a 24-hour incubation period. Given the more acidic nature of the tumor microenvironment and the presence of elevated ATP due to cellular activity,[61,62] ZIF-90 is expected to disassemble upon uptake by cells, thereby facilitating targeted drug release. An MTT assay was used to assess the viability of 4T1 cells. The experimental data revealed a high viability of approximately 90% in cells co-cultured with DOX-free ZIF-90, indicating minimal inherent cytotoxicity. However, following DOX encapsulation within ZIF-90, cell viability significantly decreased to below 50% (Fig. 3f), demonstrating that ZIF-90 effectively released its DOX payload, resulting in cell death. These findings substantiate the nanomotor's capacity to transport therapeutic agents and to

release them in response to tumor cell-specific conditions, achieving targeted cytotoxicity.

After establishing the nanomotor's motility and its capability to induce tumor cell death, the next step is to evaluate its ability to penetrate the extracellular matrix. To validate the enzymatic activity of collagenase conjugated to the nanomotors, a gelatin degradation assay was employed using FITC as a fluorescence probe. Due to aggregation-induced quenching, the fluorescence of FITC was substantially suppressed upon binding with gelatin. Upon enzymatic degradation of gelatin by collagenase, FITC is released, resulting in fluorescence recovery. When the FITC-quenched gelatin was incubated with varying concentrations of nanomotors, a concentration-dependent increase in fluorescence intensity was observed. These results confirm that the collagenase immobilized on the surface of the ZIF-90 nanomotors retained its catalytic activity and effectively degraded the gelatin matrix (Fig. S14, ESI†). Nanomotors were collected following co-incubation with gelatin, during which they had degraded the gelatin matrix. These nanomotors were then centrifuged and dried for XRD analysis. The XRD results showed no significant structural changes, indicating that the nanomotors maintained their structural integrity during the penetration process (Fig. S15, ESI†). Given that type I collagen is the primary component of the extracellular matrix,[63] a collagen membrane was established. From the SEM images of the as synthesized collagen membrane (Fig. 4b and Fig. S16, ESI†), it is evident that the fabricated collagen film is intact and densely structured, with a smooth surface. Cross-sectional SEM imaging indicates that the thickness of the dry film is approximately 1.5 μm. The Transwell coated with the collagen film was placed in a 24-well plate, and an aqueous solution containing DOX-loaded ZIF-90 nanomotors and H_2O_2 was introduced into the upper chamber of the Transwell. Concurrently, 4T1 cells were cultured at the bottom of the 24-well plate (Fig. 4a and Fig. S17, ESI†). After 24 hours, the collagen film was retrieved, rinsed, and dried for SEM observation. On the top surface of the film, where the nanomotors were applied, the surface exhibited significant roughening with visible macropores, many of which contained nanomotor particles residing within them (Fig. 4ci). This change in surface morphology is likely

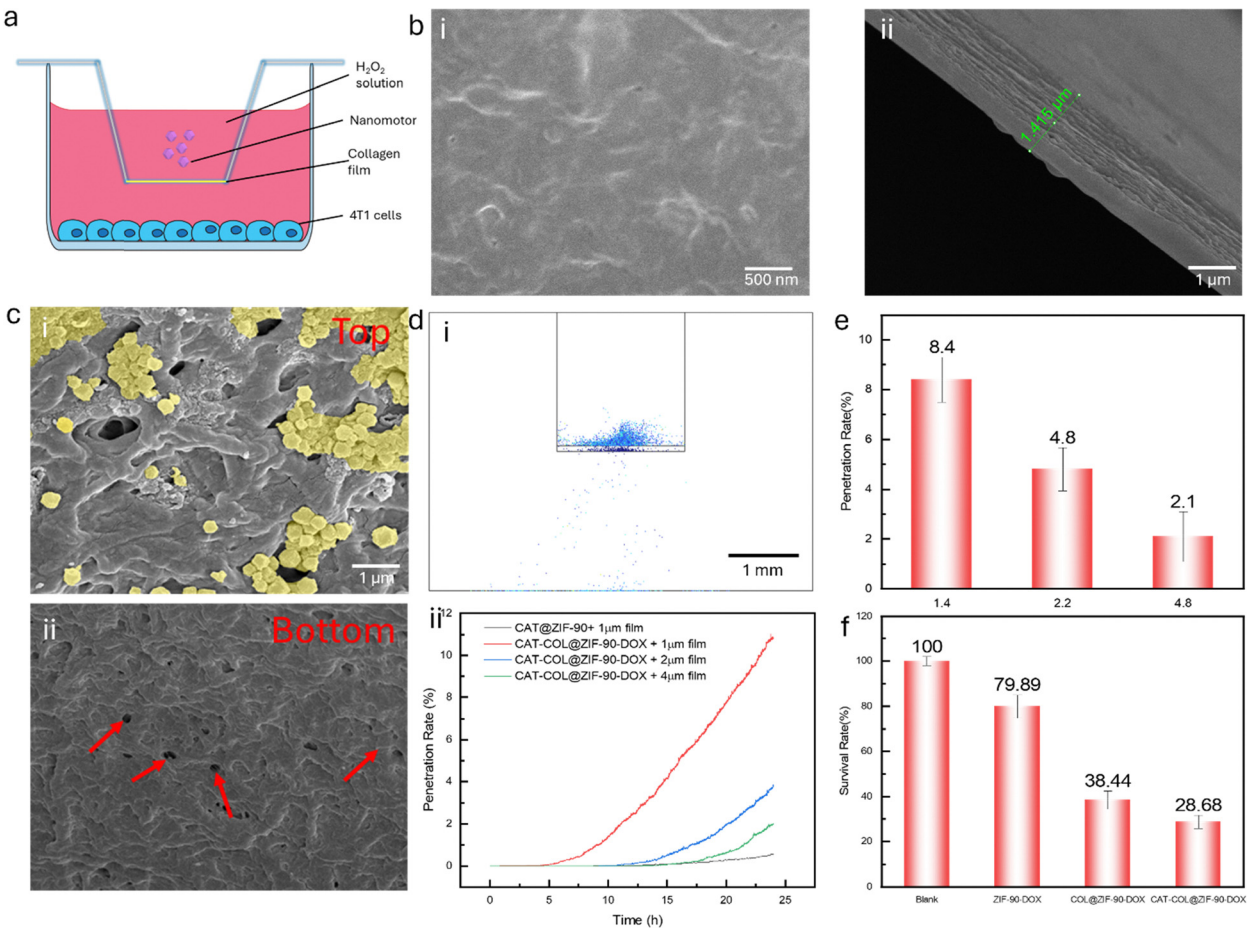

Fig. 4 (a) Schematic illustration of the customized setup designed to evaluate the penetration of collagen membranes by nanomotors. (b) SEM images of the as-synthesized collagen films (i, top view; ii, cross-sectional view). (c) SEM images of collagen films after the addition of nanomotors (i, top surface; ii, bottom surface). (d) FEM simulations of the nanomotor penetration process through the collagen film, including (i) screenshot of the numerical model setup and (ii) the simulated relationship between penetration rate and time of collagen films at various thicknesses. (e) The correlation between collagen film thickness (μm) and the penetration efficiency of nanomotors. (f) Survival rate of 4T1 cells after treatment with different ZIF-90 particles.

attributed to the enzymatic degradation of the collagen by collagenase present on the nanomotor surfaces. Additionally, numerous nanomotors remained embedded in the surface, indicating particles that initiated penetration but did not fully traverse the film. When the collagen film was inverted, multiple macropores were observed on the underside, providing further evidence of successful penetration by the nanomotors (Fig. 4cii). As a control, collagen films treated with an aqueous solution containing H_2O_2 without nanomotors, or with ZIF-90-DOX or CAT@ZIF-90-DOX, exhibited no noticeable damage (Fig. S18, ESI†), further verifying that the enhanced penetration is attributed to the active motion and enzymatic degradation facilitated by the nanomotors.

An *in silico* investigation based on the finite element method (FEM) was conducted to examine how collagenase-functionalized nanomotors penetrate collagen films, with a particular focus on how film thickness influences penetration efficiency (Fig. S19, ESI†).[64] To investigate the relationship between collagen film thickness and the penetration capability of nanomotors, we first established model parameters using experimental data on nanomotor penetration through a 1 μm collagen film (Fig. 4d). The simulation yielded a penetration rate of approximately 10%, consistent with the experimental results. Subsequently, the collagen film thickness was varied in the simulations. For a 2 μm film, the penetration rate was approximately 4%, while for a 4 μm film, it decreased to around 2% (Fig. S20, ESI†). To experimentally validate these findings, the residual culture medium was collected, and the nanomotors were dissolved using EDTA. The DOX fluorescence intensity was then measured to quantify the percentage of nanomotors that had successfully penetrated through the collagen membrane. The experimental data aligned closely with the simulation results, demonstrating that approximately 8% of the nanomotors successfully entered the culture medium. However, when the thickness of the collagen film was increased threefold, the penetration efficiency dropped significantly, with only 2% of the nanomotors successfully traversing the film (Fig. 4e). Since the concentration of hydrogen peroxide in tumor tissues is approximately 10–100 μM, we conducted a comparative experiment using a 2 μm-thickness collagen membrane model with water and 100 μM H_2O_2 solution. The results showed that the nanomotor exhibited a penetration efficiency of approximately 4.8% in the H_2O_2 solution, which was significantly higher than the 2.8% observed in water (Fig. S21, ESI†). This confirms that even low concentrations of hydrogen peroxide, as found in tumor tissues, can enhance the ability of nanomotors to penetrate the ECM.

Next, an MTT assay was conducted to evaluate cell viability, assessing the effectiveness of DOX-loaded nanomotors in inducing cell death after penetrating the collagen membrane (Fig. 4d). The results indicated that the introduction of DOX-loaded pure ZIF-90 particles (ZIF-90-DOX) led to a minor reduction in 4T1 cell viability, with approximately 80% of cells remaining viable. This minimal effect is likely due to the limited release of DOX, as the pristine ZIF-90 particles are unable to effectively penetrate the collagen membrane. The introduction of collagenase-functionalized ZIF-90-DOX (COL@ZIF-90-DOX) markedly reduced cell viability to approximately 38%. This pronounced effect highlights the role of enzymatic degradation of the collagen membrane by collagenase, which enhances the ability of nanomotors to deliver DOX effectively to the target cells. In contrast, when catalase was incorporated into the system (CAT-COL@ZIF-90-DOX), cell viability decreased further to approximately 28%. This further reduction in cell viability underscores the importance of active propulsion, facilitated by catalase, in improving the penetration efficiency through the ECM barrier.

After verifying the ability of the nanomotors in penetrating collagen membranes, a three-dimensional (3D) tumor model was established. To mimic solid tumor tissue, 4T1 cell spheroids were established using Matrigel within 24-well plates. Drug-loaded nanomotors were then added to the culture medium and incubated for 24 hours (Fig. 5a). After incubation, the wells were washed to remove unbound particles, and the Matrigel was dissolved using a collagenase solution. The fluorescence intensity of DOX in the resulting solution was measured to quantify drug release, serving as an indirect indicator of the nanomotors' penetration efficiency within the spheroids. These results revealed that only ~4% of DOX was released from standard ZIF-90 nanoparticles in the Matrigel. In contrast, a remarkable 75% increase in drug release was observed with the CAT-COL@ZIF-90-DOX nanomotors, highlighting their superior penetration capability within the spheroids (Fig. 5b and Fig. S22, ESI†). Subsequently, the cell viability within the spheroids was assessed by dissolving Matrigel with collagenase solution followed by the MTT assay (Fig. 5c). The results revealed that the introduction of DOX-loaded ZIF-90 nanoparticles maintained cell viability at 78%, indicating limited therapeutic efficacy due to insufficient penetration. In contrast, treatment with CAT-COL@ZIF-90-DOX nanomotors significantly reduced 4T1 cell viability to 45%, highlighting their superior penetration capability. This enhanced penetration is attributed to the nanomotors' dual functionalities: biocatalytic degradation of the ECM and self-propulsion, which together facilitated efficient delivery and release of the encapsulated DOX within the spheroids.

To further investigate the drug delivery efficiency, 4T1 spheroids cultured with different nanomotor formulations were analyzed using CLSM (Fig. 5d and e). Fluorescence staining was employed to differentiate between live and dead cells, where live cells exhibited green fluorescence, and dead cells were marked by blue fluorescence. In the control group treated with ZIF-90-DOX, the nanoparticles were unable to penetrate the Matrigel. Bright-field imaging identified cell clusters within the Matrigel, but fluorescence imaging revealed only green fluorescence, indicating that the cells remained viable. No DOX fluorescence was detected, confirming that the drug was not delivered to the cells (Fig. 5d). In contrast, the experimental group treated with CAT-COL@ZIF-90-DOX demonstrated significant drug delivery and cytotoxic effects. A higher-magnification view highlighted DOX fluorescence (red) co-localized with the blue fluorescence of dead cells (Fig. 5e). This co-localization confirms

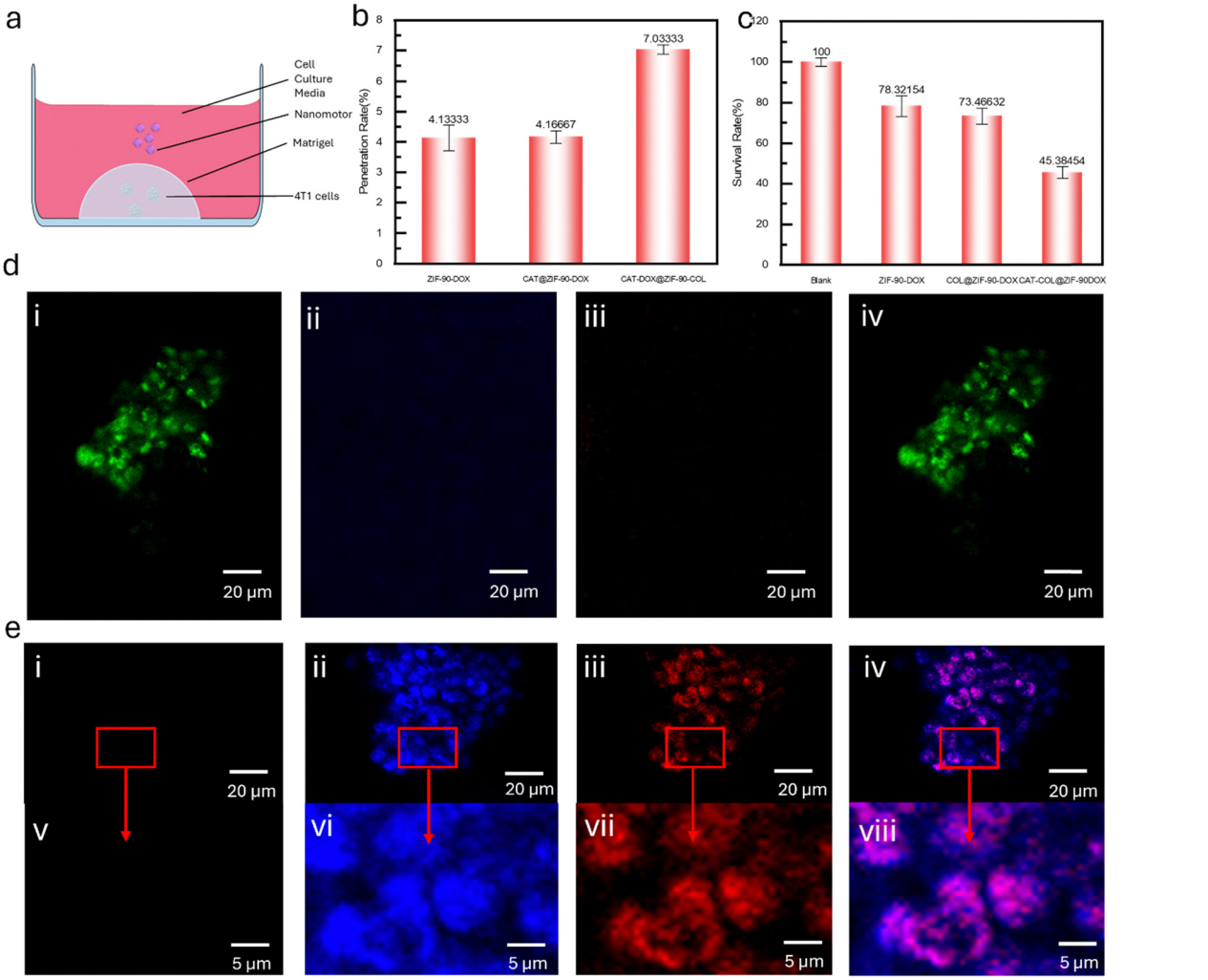

Fig. 5 (a) Schematic illustration of the 3D spheroid model used for penetration studies. (b) Penetration rates of different ZIF-90 nanomotors in the 3D spheroid model. (c) 3D spheroid cell viability after treatment with various ZIF-90 formulations. (d) and (e) CLSM images of 4T1 spheroids treated with (d) ZIF-90-DOX and (e) CAT-COL@ZIF-90-DOX. Images showing live cell staining (i), dead cell staining (ii), DOX fluorescence (iii), and merged overlays of all signals (iv). v–viii are enlarged views of i–iv from (e).

that the nanomotors effectively penetrated the spheroid, delivered DOX into the cells, and induced cytotoxicity. Experiments conducted with blank ZIF-90 and CAT@ZIF-90-DOX showed that neither was capable of killing 4T1 cells in the spheroids (Fig. S23–S24, ESI†).

Conclusions

In conclusion, we successfully synthesized dual-enzyme-functionalized nanomotors capable of self-propulsion and biocatalytic collagen degradation to enhance their motility within the ECM. Upon encountering cancer cells, the nanomotors efficiently released the encapsulated drug. In an elevated hydrogen peroxide environment, the nanomotors exhibited efficient penetration through a collagen membrane within 24 hours, resulting in the death of over 70% of 4T1 cells. In a more physiologically relevant 3D spheroid model, the nanomotors demonstrated similar efficacy, eliminating over 50% of cancer cells within the same timeframe. These nanoparticles showed improved penetration through cancerous tissues, thereby enhancing the targeted delivery of therapeutic agents to cancer cells. These findings highlight the potential of enzyme-powered nanomotors to enhance drug delivery in cancer therapy by overcoming key biological barriers such as the ECM. Further research will be valuable in optimizing these nanomotors for clinical use, particularly by studying their behavior and effectiveness in more complex *in vivo* environments.

Data availability

The authors confirm that the data supporting the findings of this study are available within the article and/or its ESI.†

Conflicts of interest

There are no conflicts to declare.

Acknowledgements

This work was supported by the Australian Research Council (FT220100479 and DP250101401) and the National Breast Cancer Foundation Australia (IIRS-22-104). The authors are grateful for the facilities' technical assistance from the Mark Wainwright Analytical Centre (MWAC) at UNSW Sydney.

References

1 D. Basak, S. Arrighi, Y. Darwiche and S. Deb, *Life*, 2022, **12**, 48.
2 F. Torino, A. Barnabei, R. Paragliola, R. Baldelli, M. Appetecchia and S. M. Corsello, *Thyroid*, 2013, **23**, 1345–1366.
3 G. Joshi, R. Sultana, J. Tangpong, M. P. Cole, D. K. Clair, M. Vore, S. Estus and D. A. Butterfield, *Free Radical Res.*, 2005, **39**, 1147–1154.
4 R. Rani, P. Malik, S. Dhania and T. K. Mukherjee, *Pharmaceutics*, 2023, **15**, 227.
5 K. Thanki, R. P. Gangwal, A. T. Sangamwar and S. Jain, *J. Controlled Release*, 2013, **170**, 15–40.
6 S. A. A. Rizvi and A. M. Saleh, *Saudi Pharm. J.*, 2018, **26**, 64–70.
7 M. M. Modena, B. Ruhle, T. P. Burg and S. Wuttke, *Adv. Mater.*, 2019, **31**, 1901556.
8 M. Morgen, C. Bloom, R. Beyerinck, A. Bello, W. Song, K. Wilkinson, R. Steenwyk and S. Shamblin, *Pharm. Res.*, 2012, **29**, 427–440.
9 H. Ragelle, F. Danhier, V. Préat, R. Langer and D. G. Anderson, *Expert Opin. Drug Delivery*, 2017, **14**, 851–864.
10 B. Begines, T. Ortiz, M. Pérez-Aranda, G. Martínez, M. Merinero, F. Argüelles-Arias and A. Alcudia, *Nanomaterials*, 2020, **10**, 1403.
11 J. W. Zhang and W. M. Saltzman, *Chem. Eng. Prog.*, 2013, **109**, 25–30.
12 J. S. Tao, S. F. Chow and Y. Zheng, *Acta Pharm. Sin. B*, 2019, **9**, 4–18.
13 N. Kamaly, B. Yameen, J. Wu and O. C. Farokhzad, *Chem. Rev.*, 2016, **116**, 2602–2663.
14 A. O. Elzoghby, W. M. Samy and N. A. Elgindy, *J. Controlled Release*, 2012, **157**, 168–182.
15 C. R. Thomas, D. P. Ferris, J. H. Lee, E. Choi, M. H. Cho, E. S. Kim, J. F. Stoddart, J. S. Shin, J. Cheon and J. I. Zink, *J. Am. Chem. Soc.*, 2010, **132**, 10623–10625.
16 Q. Yuan, J. Shah, S. Hein and R. D. K. Misra, *Acta Biomater.*, 2010, **6**, 1140–1148.
17 R. Liu, C. Luo, Z. Q. Pang, J. M. Zhang, S. B. Ruan, M. Y. Wu, L. Wang, T. Sun, N. Li, L. Han, J. J. Shi, Y. Y. Huang, W. S. Guo, S. J. Peng, W. H. Zhou and H. L. Gao, *Chin. Chem. Lett.*, 2023, **34**, 107518.
18 Z. M. Zhao, A. Ukidve, J. Kim and S. Mitragotri, *Cell*, 2020, **181**, 151–167.
19 E. Henke, R. Nandigama and S. Ergün, *Front. Mol. Biosci.*, 2020, **6**, 160.
20 J. C. Huang, L. L. Zhang, D. L. Wan, L. Zhou, S. S. Zheng, S. Z. Lin and Y. T. Qiao, *Signal Transduction Targeted Ther.*, 2021, **6**, 153.
21 T. Stylianopoulos, M. Z. Poh, N. Insin, M. G. Bawendi, D. Fukumura, L. L. Munn and R. K. Jain, *Biophys. J.*, 2010, **99**, 1342–1349.
22 T. Wolfram, J. P. Spatz and R. W. Burgess, *BMC Cell Biol.*, 2008, **9**, 64.
23 D. Cahn, A. Stern, M. Buckenmeyer, M. Wolf and G. A. Duncan, *ACS Nano*, 2024, **18**, 32045–32055.
24 S. Wilhelm, A. J. Tavares, Q. Dai, S. Ohta, J. Audet, H. F. Dvorak and W. C. W. Chan, *Nat. Rev. Mater.*, 2016, **1**, 16014.
25 M. Torrice, *ACS Cent. Sci.*, 2016, **2**, 434–437.
26 J. Katuri, X. Ma, M. M. Stanton and S. Sánchez, *Acc. Chem. Res.*, 2017, **50**, 2–11.
27 J. Y. Kim, S. Jeon, J. Lee, S. Lee, J. Lee, B. O. Jeon, J. E. Jang and H. Choi, *Sens. Actuators, B*, 2018, **266**, 276–287.
28 C. Peters, M. Hoop, S. Pané, B. J. Nelson and C. Hierold, *Adv. Mater.*, 2016, **28**, 533–538.
29 N. R. Hu, L. F. Wang, W. H. Zhai, M. M. Sun, H. Xie, Z. G. Wu and Q. He, *Macromol. Chem. Phys.*, 2018, **219**, 1700540.
30 U. Bozuyuk, O. Yasa, I. C. Yasa, H. Ceylan, S. Kizilel and M. Sitti, *ACS Nano*, 2018, **12**, 9617–9625.
31 X. H. Yan, J. B. Xu, Q. Zhou, D. D. Jin, C. A. Vong, Q. Feng, D. H. L. Ng, L. Bian and L. Zhang, *Appl. Mater. Today*, 2019, **15**, 242–251.
32 X. Wang, J. Cai, L. L. Sun, S. Zhang, D. Gong, X. H. Li, S. H. Yue, L. Feng and D. Y. Zhang, *ACS Appl. Mater. Interfaces*, 2019, **11**, 4745–4756.
33 R. Eelkema, M. M. Pollard, J. Vicario, N. Katsonis, B. S. Ramon, C. W. M. Bastiaansen, D. J. Broer and B. L. Feringa, *Nature*, 2006, **440**, 163.
34 Q. F. Chen and K. Liang, *Adv. Sens. Res.*, 2023, **2**, 2300056.
35 M. A. Ramos-Docampo, M. Fernández-Medina, E. Taipaleenmäki, O. Hovorka, V. Salgueiriño and B. Städler, *ACS Nano*, 2019, **13**, 12192–12205.
36 Y. Q. You, D. D. Xu, X. Pan and X. Ma, *Appl. Mater. Today*, 2019, **16**, 508–517.
37 M. L. Liu, L. Chen, Z. W. Zhao, M. C. Liu, T. C. Zhao, Y. Z. Ma, Q. Y. Zhou, Y. S. Ibrahim, A. A. Elzatahry, X. M. Li and D. Y. Zhao, *J. Am. Chem. Soc.*, 2022, **144**, 3892–3901.
38 P. Dhar, S. Narendren, S. S. Gaur, S. Sharma, A. Kumar and V. Katiyar, *Int. J. Biol. Macromol.*, 2020, **158**, 1020–1036.
39 S. Campuzano, B. E. F. de Avila, P. Yáñez-Sedeño, J. M. Pingarrón and J. Wang, *Chem. Sci.*, 2017, **8**, 6750–6763.
40 S. Rezvantalab, N. I. Drude, M. K. Moraveji, N. Güvener, E. K. Koons, Y. Shi, T. Lammers and F. Kiessling, *Front. Pharmacol.*, 2018, **9**, 1260.
41 M. Luo, Y. Z. Feng, T. W. Wang and J. G. Guan, *Adv. Funct. Mater.*, 2018, **28**, 1706100.
42 H. Ceylan, I. C. Yasa, O. Yasa, A. F. Tabak, J. Giltinan and M. Sitti, *ACS Nano*, 2019, **13**, 3353–3362.
43 J. Llacer-Wintle, A. Rivas-Dapena, X. Z. Chen, E. Pellicer, B. J. Nelson, J. Puigmartí-Luis and S. Pané, *Adv. Mater.*, 2021, **33**, 2102049.
44 J. E. Wu, B. J. Jang, Y. Harduf, Z. Chapnik, Ö. B. Avci, X. Z. Chen, J. Puigmartí-Luis, O. Ergeneman, B. J. Nelson, Y. Or and S. Pané, *Adv. Sci.*, 2021, **8**, 2004458.

45 L. Schaefer and D. P. Reinhardt, *Adv. Drug Delivery Rev.*, 2016, **97**, 1–3.
46 M. J. Ernsting, M. Murakami, A. Roy and S. D. Li, *J. Controlled Release*, 2013, **172**, 782–794.
47 T. Stylianopoulos and R. K. Jain, *Proc. Natl. Acad. Sci. U. S. A.*, 2013, **110**, 18632–18637.
48 V. P. Chauhan, T. Stylianopoulos, J. D. Martin, Z. Popovic, O. Chen, W. S. Kamoun, M. G. Bawendi, D. Fukumura and R. K. Jain, *Nat. Nanotechnol.*, 2012, **7**, 383–388.
49 M. M. Wan, H. Chen, Q. Wang, Q. Niu, P. Xu, Y. Q. Yu, T. Y. Zhu, C. Mao and J. Shen, *Nat. Commun.*, 2019, **10**, 14–21.
50 J. Z. Wang, Z. Xiong, X. J. Zhan, B. H. Dai, J. Zheng, J. Liu and J. Y. Tang, *Adv. Mater.*, 2017, **29**, 1701451.
51 A. D. Fusi, Y. D. Li, A. Llopis-Lorente, T. Patino, J. C. M. van Hest and L. K. E. A. Abdelmohsen, *Angew. Chem., Int. Ed.*, 2023, **62**, e202214754.
52 J. Z. Wang, Z. Xiong, J. Zheng, X. J. Zhan and J. Y. Tang, *Acc. Chem. Res.*, 2018, **51**, 1957–1965.
53 F. X. Gu, R. Karnik, A. Z. Wang, F. Alexis, E. Levy-Nissenbaum, S. Hong, R. S. Langer and O. C. Farokhzad, *Nano Today*, 2007, **2**, 14–21.
54 C. M. J. Hu, L. Zhang, S. Aryal, C. Cheung, R. H. Fang and L. F. Zhang, *Proc. Natl. Acad. Sci. U. S. A.*, 2011, **108**, 10980–10985.
55 M. Vanderrest and R. Garrone, *FASEB J.*, 1991, **5**, 2814–2823.
56 F. K. Shieh, S. C. Wang, S. Y. Leo and K. C. W. Wu, *Chem. – Eur. J.*, 2013, **19**, 11139–11142.
57 M. Z. Gao, J. Wang, Z. H. Rong, Q. Shi and J. X. Dong, *RSC Adv.*, 2018, **8**, 39627–39634.
58 J. Yong, K. Hakobyan, J. T. Xu, A. S. Mellick, J. Whitelock and K. Liang, *Biotechnol. J.*, 2023, **18**, 2300015.
59 X. Ma, A. Jannasch, U. R. Albrecht, K. Hahn, A. Miguel-Lopez, E. Schaffer and S. Sanchez, *Nano Lett.*, 2015, **15**, 7043–7050.
60 X. Ma and S. Sánchez, *Tetrahedron*, 2017, **73**, 4883–4886.
61 K. G. de la Cruz-López, L. J. Castro-Muñoz, D. O. Reyes-Hernández, A. García-Carrancá and J. Manzo-Merino, *Front. Oncol.*, 2019, **9**, 1143.
62 M. Hosonuma and K. Yoshimura, *Front. Oncol.*, 2023, **13**, 1175563.
63 B. Sun, *Cell Rep. Phys. Sci.*, 2021, **2**, 100515.
64 H. Liu, *Adv. Eng. Technol. Res.*, 2024, **12**, 755–764.